A hybrid ice-mélange model based on particle and continuum methods

Saskia Kahl[1], Carolin Mehlmann[1], and Dirk Notz[2]

[1]Institute of Analysis and Numerics, Otto-von-Guericke Universität, Magdeburg, Germany
[2]Center for Earth System Research and Sustainability (CEN), Institute of Oceanography, Universität Hamburg, Germany

Correspondence: Saskia Kahl (saskia.kahl@ovgu.de)

Abstract. Ice mélange, a composite of sea ice and icebergs, can have a major influence on sea-ice-ocean interactions. However, ice mélange could so far not be represented in climate models because numerically efficient realizations did not exist. This motivates the development of a prototype dynamic hybrid ice-mélange model that we present in this paper. In our approach, icebergs are included as particles while sea ice is treated as a continuum. To derive a joint continuum for the ice mélange, we integrate particle properties into the sea-ice continuum. Thus, icebergs are viewed as thick, compact pieces of sea ice. The ice-mélange formulation is derived based on the viscous-plastic sea-ice rheology, which is currently the most widely used material law for sea ice in climate models. Starting from the continuum mechanical formulation, we modify the rheology such that icebergs are held together by a modified tensile strength in the material law. Due to the particle approach, we do not need high resolved spatial meshes to represent the typical size of icebergs in ice mélange (< 300 m). Instead, icebergs can be tracked on a subgrid level while the typical resolution of the sea-ice model can be maintained ($\geq$10 km). This is an appealing property in respect to computational efficiency. Applying idealized test cases, we demonstrate that the proposed changes in the material law allow for a realistic representation of icebergs within the viscous-plastic sea-ice rheology. Furthermore, we show that subgrid dynamics, such as polynya formation due to grounded icebergs, can be modelled with the hybrid approach. Overall, this suggested extension of the viscous-plastic sea-ice model is a promising path towards the integration of ice mélange into climate models.

1 Introduction

Fjords with marine terminating glaciers are commonly found in the polar regions, for example around Greenland. These fjord systems can be filled with sea ice into which icebergs calve, so that a mixture of sea ice, bergy bits and icebergs is formed: *ice mélange*. The ice mélange consists of many interacting small icebergs (< 300 m) (Dowdeswell et al., 1992; Sulak et al., 2017). Observations based on field campaigns and remote sensing data indicate that ice mélange affects the glacier-fjord system either by releasing fresh water into the fjord (Enderlin et al., 2018; Mortensen et al., 2020; Moon et al., 2018) or by creating a force at the glacier termini (Cassotto et al., 2015; Bevan et al., 2019; Xie et al., 2019). The latter might be strong enough that it prevents calving events (e.g. Amundson et al., 2010; Krug et al., 2015; Bassis et al., 2015), whereas the release of fresh water through icebergs influences the fjord circulation and the melting at the glacier termini (Davison et al., 2020).

25   Observing ice mélange is difficult, due to the sparsity of remote sensing data and due to the challenges of taking in-situ measurements. To obtain insights into the potential impact of ice mélange on glacier calving and the underlying ocean circulation, numerical models are therefore necessary. The existing approaches used to include ice mélange into models vary in their complexity. They range from the full description of the ice-mélange dynamics to the parameterization of specific interactions such as the load which the ice mélange creates at the glacier termini (Schlemm and Levermann, 2021).

30   There are two distinct approaches in the scientific literature to model the dynamics of ice-mélange: in particle methods the ice mélange is expressed using discrete interacting particles, with single particles representing icebergs or sea-ice floes (e.g. Robel, 2017; Burton et al., 2018). As discussed by Vaňková and Holland (2017) implementing a full particle approach into climate models would be extremely challenging due to the enormous numerical costs. In contrast, in the continuum approach, the ice mélange is prescribed as a single continuum (e.g. Pollard et al., 2018; Amundson et al., 2024).

35   To provide a simple coupling between ice-mélange and sea-ice modules used in climate models, Vaňková and Holland (2017) introduced a continuum ice-mélange model, where sea ice and icebergs build a joint continuum. Icebergs are represented via thick compact pieces of sea ice, which are tracked with a Lagrangian advection using moving meshes. In their model the icebergs are held together via a large tensile and shear strength, which is introduced by a modification of the underlying cavitating fluid sea-ice rheology (Flato and Hibler, 1992). The approach of Vaňková and Holland (2017) requires a high spatial
40   resolution to resolve icebergs in the ice mélange. As the momentum equation of the underlying sea-ice model is nonlinear, solving such types of equation is numerically challenging (Koldunov et al., 2019; Mehlmann and Richter, 2017b). So far, efficient solvers for the ice-mélange model of Vaňková and Holland (2017) are missing.

To overcome these difficulties, we here introduce a hybrid ice-mélange model. In this approach, the ice mélange is described as a joint continuum consisting of sea ice (continuum) and icebergs (particles). The use of particles in the hybrid approach
45   allows us to track the icebergs on a subgrid level. This has the advantage that icebergs do not need to be resolved by the spatial mesh. Thus, the grid of the sea-ice model, with its typical grid size of several kilometres in climate models, can be used to simulate ice mélange. We derive the momentum equation of the ice mélange by selectively modifying the tensile strength of the sea-ice rheology. This concept is similar to the approach of Vaňková and Holland (2017), but instead of applying the cavitating fluid sea-ice rheology, we consider the viscous-plastic (Hibler, 1979) material law, which has been shown to be more realistic
50   than the cavitating fluid model (Kreyscher et al., 2000).

So far, most climate models treat sea ice as a viscous-plastic material using the viscous-plastic (Hibler, 1979) or elastic-viscous-plastic (Hunke, 2001) sea-ice rheology. These rheologies are used in 30 out of the 33 global climate models of the Climate Model Intercomparison Project 5 (CMIP5) (Stroeve et al., 2014). Furthermore, the study of Amundson and Burton (2018) indicates that ice mélange exhibits viscous-plastic deformations. Thus, an inclusion of ice mélange into climate models
55   via a modification of the viscous-plastic material law is a promising approach.

The paper is structured as follows: Section 2 presents the ice-mélange model and Section 3 outlines the used numerical discretization. The model is numerically evaluated in Section 4. We discuss our results in Section 5 and summarize our conclusions in Section 6.

2 Viscous-plastic ice-mélange model

Based on the representation of the sea-ice dynamics with a viscous-plastic rheology, we develop a model for ice mélange. As in the underlying sea-ice model (Hibler, 1979), the ice-mélange model consists of three prognostic variables: the ice-mélange's thickness H, its concentration A within a specific grid cell, and horizontal velocity $\boldsymbol{v}$. The ice mélange is considered as a joint continuum of sea ice and icebergs, where icebergs are prescribed as thick and compact pieces of ice. When modelling the ice mélange, we take advantage of the fact that icebergs are significantly thicker than sea ice (Dowdeswell et al., 1992; Sulak et al., 2017). Thus, the thickness and concentration of ice mélange can be described as

$$H(x,y,t) = \begin{cases} H_{ice}(x,y,t) & \text{if} \quad p(x,y,t) \notin (x,y) \in \Omega, \\ H_{ice}(x,y,t) + h_p & \text{if} \quad p(x,y,t) \in (x,y) \in \Omega. \end{cases} \tag{1}$$

$$A(x,y,t) = \begin{cases} A_{ice}(x,y,t) & \text{if} \quad p(x,y,t) \notin (x,y) \in \Omega, \\ 1 & \text{if} \quad p(x,y,t) \in (x,y) \in \Omega. \end{cases} \tag{2}$$

Here, Ω is the two dimensional domain of interest, x and y are the horizontal spatial coordinates, t the time, $p(x,y,t)$ is the particle and h_p describes the iceberg thickness. In order to model the ice-mélange velocity we formulate an expansion of the viscous-plastic rheology that accounts for icebergs. To keep icebergs (thick and concentrated pieces of ice) in the ice-mélange formulation together, we modify the tensile strength of the viscous-plastic law.

In the following, we first generally review the formulation of the governing equations (Section 2.1) and the viscous-plastic rheology (Section 2.2), before we modify its strength parameterization (2.3) to represent icebergs. The iceberg particle interaction and the coupling to the continuum ice-mélange formulation is outlined in Section 2.4.

2.1 Momentum and conservation equation

The drift of the ice mélange is described by the two-dimensional momentum equation

$$\rho H \partial_t \boldsymbol{v} = \nabla \cdot \boldsymbol{\sigma} + F_b, \tag{3}$$

where $\rho = 900 \ \mathrm{kg m^{-3}}$ is the mass per unit area and $\nabla \cdot \boldsymbol{\sigma}$ describes the divergence of the two-dimensional symmetric stress tensor. The internal stresses are given by the material law described in Section 2.3. The remaining terms collected in F_b,

$$F_b = -\rho H f k \times \boldsymbol{v} - \rho H g \nabla H_d + \tau_{atm} - \tau_{\mathrm{ocean}}(\boldsymbol{v}), \tag{4}$$

model the body forces acting on the ice mélange: the Coriolis parameter f with upward pointing unit vector k, the gravity constant g, the surface height H_d, and the atmospheric and oceanic stresses given by τ_{atm} and τ_{ocean}. These two drag terms (Coon, 1980) are expressed as

$$\tau_{atm} = C_{\mathrm{atm}} \rho_{\mathrm{atm}} \|\boldsymbol{v}_{\mathrm{atm}}\|_2 (\boldsymbol{v}_{\mathrm{atm}}), \tag{5}$$

$$\tau_{ocean}(\boldsymbol{v}) = C_{\mathrm{ocean}} \rho_{\mathrm{ocean}} \|\boldsymbol{v} - \boldsymbol{v}_{\mathrm{ocean}}\|_2 (\boldsymbol{v} - \boldsymbol{v}_{\mathrm{ocean}}), \tag{6}$$

where $\boldsymbol{v}_{\mathrm{atm}}$ describes the wind velocity and $\boldsymbol{v}_{\mathrm{ocean}}$ the ocean current. The corresponding densities are given by $\rho_{\mathrm{atm}} = 1.3 \ \mathrm{kgm}^{-3}$ and $\rho_{\mathrm{ocean}} = 1026 \ \mathrm{kgm}^{-3}$. The drag coefficients are $C_{\mathrm{atm}} = 1.2 \ \times 10^{-3}$ and $C_{\mathrm{ocean}} = 5.5 \times 10^{-3}$. Note that $\|\cdot\|_2$ is the Euclidean norm. The advection of the ice-mélange thickness H and concentration A are calculated as

$$\partial_t H + \mathrm{div}(H\boldsymbol{v}) = S_{\mathrm{H}},$$
$$\partial_t A + \mathrm{div}(A\boldsymbol{v}) = S_{\mathrm{A}}, \tag{7}$$

with $H \in [0, \infty)$ and $A \in [0,1]$. For the sake of simplicity we set the thermodynamic source terms S_{H} and S_{A} in the numerical examples to zero.

2.2 Viscous-plastic rheology

Let $\tilde{\boldsymbol{\sigma}}$ be the principle components of the stress tensor $\boldsymbol{\sigma}$ given by

$$\tilde{\boldsymbol{\sigma}}_1 = \frac{\boldsymbol{\sigma}_{11} + \boldsymbol{\sigma}_{22}}{2} + \sqrt{\left(\frac{\boldsymbol{\sigma}_{11} - \boldsymbol{\sigma}_{22}}{2}\right)^2 + \boldsymbol{\sigma}_{12}^2},$$
$$\tilde{\boldsymbol{\sigma}}_2 = \frac{\boldsymbol{\sigma}_{11} + \boldsymbol{\sigma}_{22}}{2} - \sqrt{\left(\frac{\boldsymbol{\sigma}_{11} - \boldsymbol{\sigma}_{22}}{2}\right)^2 + \boldsymbol{\sigma}_{12}^2}. \tag{8}$$

In the viscous-plastic model (Hibler, 1979), the states of the stress $\boldsymbol{\sigma}$ are described by an elliptic yield curve of the form

$$F(\tilde{\boldsymbol{\sigma}}_1, \tilde{\boldsymbol{\sigma}}_2) = \left(\frac{\tilde{\boldsymbol{\sigma}}_1 + \tilde{\boldsymbol{\sigma}}_2 + P}{P}\right)^2 + \left(\frac{\tilde{\boldsymbol{\sigma}}_1 - \tilde{\boldsymbol{\sigma}}_2}{P}e\right)^2 - 1 = 0, \tag{9}$$

where $e = 2$ is the minor axis of the ellipse and P is the ice strength modelled as

$$P = P^\star H \exp(-C(1 - A)), \tag{10}$$

with strength parameter $P^\star = 27.5 \times 10^3 \ \mathrm{Nm}^{-2}$ and $C = 20$. The yield curve is expressed in terms of the principal components of the stress tensor $\boldsymbol{\sigma}$

$$\tilde{\boldsymbol{\sigma}}_1 = \frac{\boldsymbol{\sigma}_{11} + \boldsymbol{\sigma}_{22}}{2} + \sqrt{\left(\frac{\boldsymbol{\sigma}_{11} - \boldsymbol{\sigma}_{22}}{2}\right)^2 + \boldsymbol{\sigma}_{12}^2},$$
$$\tilde{\boldsymbol{\sigma}}_2 = \frac{\boldsymbol{\sigma}_{11} + \boldsymbol{\sigma}_{22}}{2} - \sqrt{\left(\frac{\boldsymbol{\sigma}_{11} - \boldsymbol{\sigma}_{22}}{2}\right)^2 + \boldsymbol{\sigma}_{12}^2}. \tag{11}$$

A visualization of the yield curve is given in Figure 1 (blue line). As there are no stress states on the yield curve with $(\tilde{\boldsymbol{\sigma}}_1, \tilde{\boldsymbol{\sigma}}_2) > 0$, sea ice has almost no tensile strength (no resistance to divergence) (Leppäranta, 2011). The stress states are related to the strain rates

$$\dot{\boldsymbol{\epsilon}}_{ij} = \frac{1}{2}\left\{\partial_{\mathbf{x}_j} \boldsymbol{v}_i + \partial_{\mathbf{x}_i} \boldsymbol{v}_j\right\}, \tag{12}$$

by the constitutive law (Hibler, 1979)

$$\boldsymbol{\sigma}_{ij} = 2\eta\dot{\boldsymbol{\epsilon}}_{ij} + (\zeta - \eta)(\dot{\boldsymbol{\epsilon}}_{11} + \dot{\boldsymbol{\epsilon}}_{22})\delta_{ij} - \frac{P}{2}\delta_{ij}, \tag{13}$$
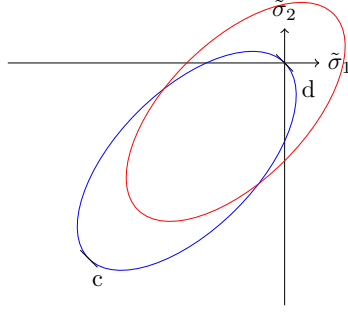
Figure 1. Two-dimensional yield curve in principal stress space without (blue) and with (red) tensile strength. Pure divergence d is in the origin of the graph, pure convergence is obtained in c. $\tilde{\boldsymbol{\sigma}}_1$ and $\tilde{\boldsymbol{\sigma}}_2$ are the principal components of the stress tensor $\boldsymbol{\sigma}$ (see Eq. (13)).

where δ_{ij} is the Kronecker symbol. The nonlinear shear ζ and bulk viscosity η are chosen as

$$\eta = e^{-2}\zeta, \quad \zeta = \frac{P}{2\Delta(\dot{\boldsymbol{\epsilon}})}. \tag{14}$$

110 To guarantee a smooth transition between the viscous and the plastic regime, we follow Kreyscher et al. (2000) and choose

$$\Delta(\dot{\boldsymbol{\epsilon}}) = \sqrt{\Delta_P(\dot{\boldsymbol{\epsilon}})^2 + \Delta_{\min}^2}. \tag{15}$$

In case of the plastic regime, $\Delta_P(\dot{\boldsymbol{\epsilon}})$ is defined as

$$\Delta_P(\dot{\boldsymbol{\epsilon}}) = \sqrt{(\dot{\boldsymbol{\epsilon}}_{11}^2 + \dot{\boldsymbol{\epsilon}}_{22}^2)(1 + e^{-2}) + 4e^{-2}\dot{\boldsymbol{\epsilon}}_{12}^2 + 2\dot{\boldsymbol{\epsilon}}_{11}\dot{\boldsymbol{\epsilon}}_{22}(1 - e^{-2})}. \tag{16}$$

The viscous regime is given as

115 $$\Delta_{\min}(\dot{\boldsymbol{\epsilon}}) = 2 \times 10^{-9}. \tag{17}$$

2.3 Strength parameterization

The absence of tensile strength in the original model is apparent from the fact that the yield curve of the viscous-plastic rheology does not contain combinations of $(\tilde{\boldsymbol{\sigma}}_1, \tilde{\boldsymbol{\sigma}}_2) > 0$ (see blue curve in Figure 1). A tensile strength has been introduced into this model for example by König and Holland (2010) to model landfast sea ice, or in the ice-mélange model based on a
120 cavitating-fluid rheology (Vaňková and Holland, 2017). Similar to Vaňková and Holland (2017), we introduce a tensile strength into the standard viscous-plastic sea-ice rheology to model icebergs. This tensile strength leads to a resistance to divergence in the presence of icebergs.

By including the tensile strength, the elliptic yield curve is shifted into the first quadrant (red curve in Figure 1). The new center of the ellipse is given by $\left(-\frac{P-T}{2}, -\frac{P-T}{2}\right)$, with the maximum tensile strength T. Both P and T are positive numbers.
125 Thus, the modified elliptic yield curve is given by

$$F(\tilde{\boldsymbol{\sigma}}_1, \tilde{\boldsymbol{\sigma}}_2) = \left(\frac{\tilde{\boldsymbol{\sigma}}_1 + \tilde{\boldsymbol{\sigma}}_2 + P - T}{P + T}\right)^2 + \left(\frac{\tilde{\boldsymbol{\sigma}}_1 - \tilde{\boldsymbol{\sigma}}_2}{P + T}e\right)^2 - 1 = 0, \tag{18}$$

with the elliptic ratio e. For $T = 0$ (no tensile strength), the elliptic yield curve is equivalent to the ellipse of the viscous-plastic sea-ice rheology (see Eq. (9)). It is assumed that ∂F and the strain rates are perpendicular to the surface of the yield curve (Leppäranta, 2011). Thus, the relation between the stress tensor and the strain rates for the shifted yield curve is derived by a normal flow rule

$$\dot{\boldsymbol{\epsilon}}_{ij} = \gamma \frac{\partial F(\boldsymbol{\sigma}_{11}, \boldsymbol{\sigma}_{22}, \boldsymbol{\sigma}_{12}, \boldsymbol{\sigma}_{21})}{\partial \boldsymbol{\sigma}_{ij}}, \tag{19}$$

with $\gamma > 0$. This leads to the modified rheology

$$\boldsymbol{\sigma}_{ij} = 2\eta \dot{\boldsymbol{\epsilon}}_{ij} + (\zeta - \eta)(\dot{\boldsymbol{\epsilon}}_{11} + \dot{\boldsymbol{\epsilon}}_{22}) \delta_{ij} - \frac{P - T}{2} \delta_{ij}, \tag{20}$$

with the bulk and shear viscosities

$$\zeta = \frac{P + T}{2\Delta}, \quad \eta = \frac{\zeta}{e^2} = \frac{P + T}{2\Delta e^2}. \tag{21}$$

Following König and Holland (2010), we define the tensile strength T relative to the compressive strength

$$T = P^\star H \Phi. \tag{22}$$

The indicator function Φ is given as

$$\Phi = \begin{cases} 0 \text{ if } p(x, y, t) \notin (x, y), \\ 1 \text{ if } p(x, y, t) \in (x, y). \end{cases} \tag{23}$$

2.4 Iceberg coupling

The icebergs are modelled via a set of particles $\{p\}$ which are placed into the sea ice. Every iceberg is represented by a disk shaped particle p, which is equipped with a radius r_p and a height h_p. The particles are advected based on the continuum ice-mélange velocity $\boldsymbol{v}$:

$$\boldsymbol{x}_p(t + \Delta t) = \boldsymbol{x}_p(t) + \int_t^{t + \Delta t} \boldsymbol{v}(\boldsymbol{x}_p(\tilde{t}), \tilde{t}) d\tilde{t}, \tag{24}$$

where $\boldsymbol{x}_p = (x_p, y_p)$ is the position of the center of particle p. An interaction of two distinct particles p_i, p_j, is modeled if the particles overlap:

$$||\boldsymbol{x}_i(t) - \boldsymbol{x}_j(t)|| \leq r_i + r_j, \tag{25}$$

with r_i, r_j being the radii and $\boldsymbol{x}_i(t) = (x_i, y_i)$ and $\boldsymbol{x}_j(t) = (x_j, y_j)$ are the positions of the interacting particles p_i and p_j, respectively. The position of the overlapping particles is corrected by assuming an inelastic collision (Herman, 2011). For this

we use the last particle position (x^*, y^*) in which the particles had not collided and update the location of the particles based on the ice-mélange velocity corrected for the collision. The latter is calculated as follows:

$$\tilde{\boldsymbol{v}}_i = \boldsymbol{v}_i - \frac{\alpha_{ij}}{m_i}, \quad \tilde{\boldsymbol{v}}_j = \boldsymbol{v}_j + \frac{\alpha_{ij}}{m_j}, \tag{26}$$

where $\boldsymbol{v}_i = \boldsymbol{v}(x_i, y_i, t)$ and $\boldsymbol{v}_j = \boldsymbol{v}(x_j, y_j, t)$ are the current velocities of the ice mélange, and m_i, m_j are the mass of particle p_i, p_j, respectively. The coefficient α_{ij} is given by

$$\alpha_{ij} = \frac{m_i m_j}{m_i + m_j} (1 + \epsilon) \cdot n_{ij} (\boldsymbol{v}_i - \boldsymbol{v}_j) n_{ij}, \tag{27}$$

with the relative unit position $n_{ij} = \frac{\boldsymbol{x}_i - \boldsymbol{x}_j}{\|\boldsymbol{x}_i - \boldsymbol{x}_j\|}$. The coefficient of restitution ϵ is set to 0.9, as this value has been used in the past for sea ice (Shen et al. (1987)). Since we assume, that icebergs are thick pieces of sea ice, this choice is appropriate.

3 Numerical discretization

The ice-mélange model is implemented in the academic software library Gascoigne (Braack et al., 2021), which uses quadrilateral grids. On the mesh, the velocity unknowns are placed at the vertices, whereas the tracers are staggered at the cell centers. This placement corresponds to an A-grid and a B-grid type staggering for the velocity and tracers, respectively. The velocity is approximated in space with piecewise linear finite elements, whereas the tracers are discretized as a piecewise constant per cell.

For the time discretization of the ice-mélange model we split the coupled system of equations in time. First, we approximate the solution of the transport equation (7). Then, the solution of the momentum equation (Eq. 3) with the updated tracers is computed. We use an implicit Euler method for the time discretization of the momentum equation. This choice is motivated by the fact that an explicit discretization of the viscous-plastic sea-ice model requires a time step of 1 s on a grid with size 100 km × 100 km (Ip et al., 1991). We expect similar constraints for the ice-mélange model, because its rheology is based on the viscous-plastic sea-ice model.

For our choice of an implicit temporal discretization, a nonlinear system of differential equations needs to be solved in every time step. We suggest to use a modified Newton method for this solution as it shows improved convergence compared to a standard Newton method and Picard solver (Mehlmann and Richter, 2017a).

3.1 Coupling between particle and continuum method

In order to derive the continuum thickness and concentration of the ice mélange, the icebergs in form of particles need to be numerically coupled into the continuum sea ice. We realize this by calculating a continuum iceberg thickness and iceberg

concentration in each cell K:

$$A_{\text{iceberg}}|_K = \sum_{p \in K} \frac{a_p}{|K|}, \tag{28}$$

$$H_{\text{iceberg}}|_K = \sum_{p \in K} \frac{\rho h_p a_p}{|K|}, \tag{29}$$

with the particle area $a_p = \pi r^2|_K$ and the area of a grid cell $|K|$. We use the iceberg concentration to determine the tensile strength in the presence of icebergs (see Eq. 22). Thus, the indicator function is given by

$$\Phi = \begin{cases} 0 \text{ if } A_{\text{iceberg}}|_K < \frac{\pi(0.5\sqrt{|K|})^2}{|K|}, \\ 1 \text{ else.} \end{cases} \tag{30}$$

The threshold is selected such that the tensile strength becomes active as soon as an area of the grid cell is covered with icebergs that cover an area at least as large as a disk shaped iceberg with radius $\sqrt{|K|}$. This choice is discussed in Section 5.

The ice-mélange concentration and thickness in each grid cell are given by

$$A|_K = \min(A_{\text{iceberg}}|_K + A_{\text{sea-ice}}|_K, 1), \tag{31}$$

$$H|_K = H_{\text{iceberg}}|_K + H_{\text{sea-ice}}|_K. \tag{32}$$

To calculate the advection of ice mélange in Eq. (7), we separately transport the continuum sea ice and the icebergs in form of particles: Sea ice is advected via an upwind-scheme, while the particles are transported according to Eq. (24) in a sub-stepping procedure. With this approach, each particle is advected with the corresponding ice-mélange velocity. The latter is given by evaluating the finite element interpolation at the particle location. After the advection step, the icebergs are checked for collision with other icebergs or with the boundary of the domain and are then replaced accordingly to Eq. (26). With the updated sea-ice tracers and particle positions, the thickness and concentration of the ice mélange are then finally calculated accordingly to Eq. (31) and Eq. (32).

4   Numerical validation

The proposed hybrid ice-mélange model is tested in five idealized test cases. The first three test cases (Section 4.1) highlight the need of introducing a tensile strength for icebergs into the viscous-plastic sea-ice rheology. Based on the verification of the modified tensile strength, we address the particle coupling in the last two test cases (Section 4.2).

4.1   Tensile strength

The first three test cases are designed such that the behaviour of the ice mélange is tested under tensile (Section 4.1.1), compressive (Section 4.1.2) and shear (Section 4.1.3) forces. For the sake of simplicity we use $v_{\text{ocean}} = 0 \text{ ms}^{-1}$. In order to reduce the complexity for the analysis of the modified tensile strength, we neglect the particle coupling in these first three test
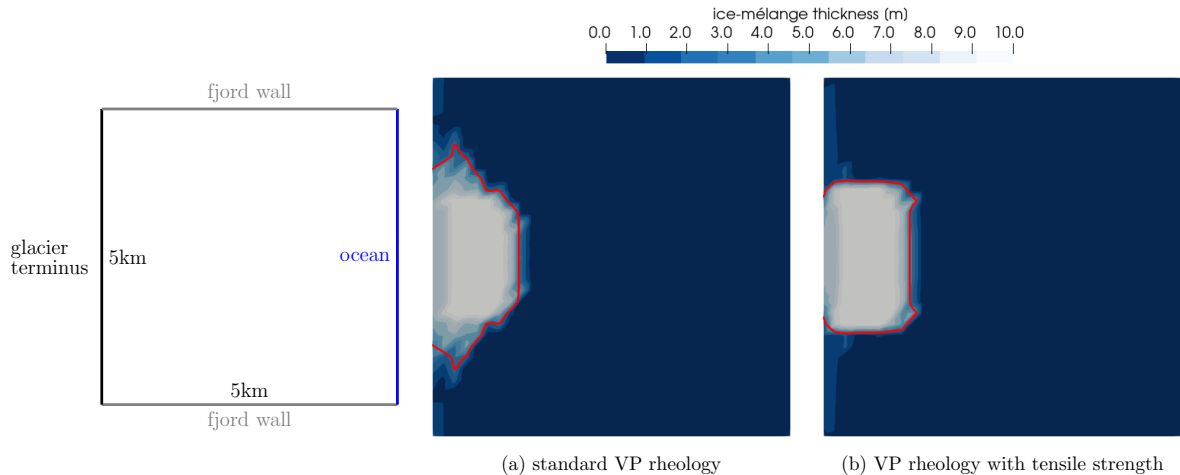
Figure 2. Visualization of the ice-mélange thickness for a test case in which an iceberg (thick red contour line) is pushed against the glacier terminus (left boundary) by a constant wind ($v_{\mathrm{atm}} = 20\ \mathrm{ms}^{-1}$). The panels denote the results for (a) the standard viscous-plastic rheology and (b) for the viscous-plastic rheology with tensile strengths. Both snapshots show the simulation result after 3 h.

cases. Instead of simulating the iceberg motion via particles and integrating it into the sea-ice continuum, we track the icebergs (thick and compact pieces of sea ice) in the sea ice via an indicator function ϕ that is transported in time:

$$\partial_t \phi + \mathrm{div}(\phi \boldsymbol{v}) = 0, \quad \phi(x,y,0) = \delta_{xy}, \tag{33}$$

where δ_{xy} is the Kronecker symbol that equals to 1 in the presence of icebergs. According to the volume-in-fluid method (Hirt and Nichols, 1982) the indicator function Φ of Eq. (22) is modified to

$$\Phi = \begin{cases} 0 \text{ if } \phi \leq c & \text{for sea ice,} \\ 1 \text{ if } \phi > c & \text{for icebergs.} \end{cases} \tag{34}$$

We haven chosen $c = 0.3$ by experimental tuning.

4.1.1 Iceberg pushed against a wall

The first test case is similar to the one used by Vaňková and Holland (2017). The domain is given by an area of the size 5 km $\times$ 5 km, see left plot in Figure 2. All boundaries except the exit to the ocean (right boundary) use Dirichlet boundary conditions ($\boldsymbol{v} = 0$). The upper and lower boundaries represent the coast lines, while the boundary on the left represents the glacier terminus. We place a 1 km $\times$ 2 km large iceberg in front of the glacier wall. A grid cells size of 110 m is used. The iceberg is a 10 m thick compact block of sea ice with a concentration of 1. The left half (< 2.5 km) of the domain is filled with 0.1 m thick sea ice with a concentration of 0.1. The iceberg is pushed against the glacier terminus through a constant wind $\boldsymbol{v}_{\mathrm{atm}} = 20\ \mathrm{ms}^{-1}$.

(a) standard VP rheology   (b) VP rheology with tensile strength
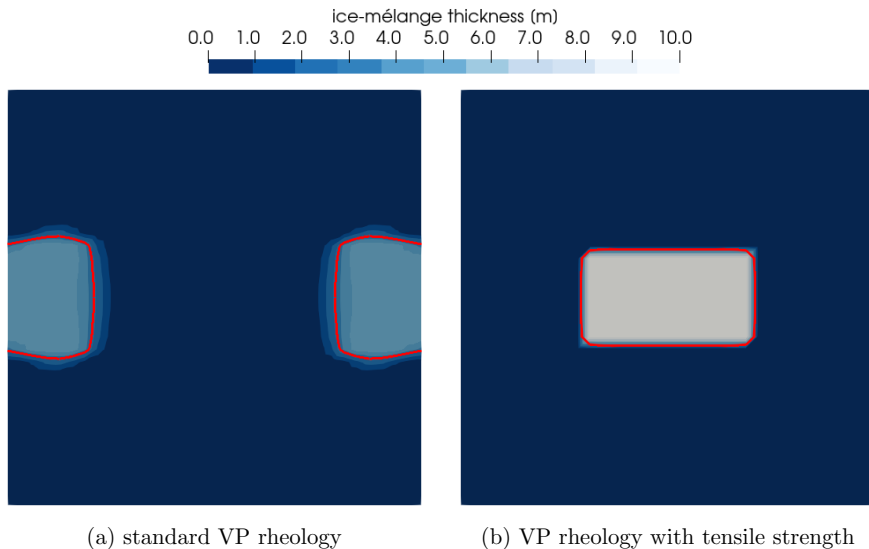
Figure 3. The iceberg (thick red contour line) is placed under a divergent wind field. The panels denote the results for (a) the standard viscous-plastic rheology and (b) for the viscous-plastic rheology with tensile strength. Both snapshots show the ice-mélange thickness after 3 h.

The simulation is run for 3 h. When comparing the standard viscous-plastic rheology and the modified material law (Figure 2), we find that for the standard viscous-plastic rheology, the thick and compact piece of sea ice, which models the iceberg, moves towards the glacier and accumulates in front of the glacier terminus. This is visible by the thick red line shown in Figure 2(a), which visualizes the iceberg's contour. With the proposed modification, the iceberg is able to keep its rectangular shape throughout the simulation (see Figure 2(b)). This test case shows that in our modified viscous-plastic rheology, the iceberg can withstand the compression, initiated by the wind forcing.

4.1.2 Iceberg under a divergent wind field

We consider a 5 km $\times$ 5 km large domain with a divergent wind field

$$
\boldsymbol{v}_{\text{atm}} = \begin{cases} 15 \text{ ms}^{-1} & x > 2.5 \text{ km}, \\ -15 \text{ ms}^{-1} & x < 2.5 \text{ km}. \end{cases} \tag{35}
$$

The 10 m thick iceberg with a concentration of 1 is placed in the middle of the domain. The whole domain is filled with sea ice whose concentration is 0.1 and whose thickness is 0.1 m. Using the standard viscous-plastic rheology, the iceberg is torn apart after 3 h (see Figure 3(a)). With additional tensile strength the iceberg keeps its form (see Figure 3(b)). The surrounding sea ice is still transported in wind direction. This test case shows in particular that the iceberg maintains its shape under diverging wind conditions at the location of the iceberg.

(a) standard VP rheology   (b) VP rheology with tensile strength
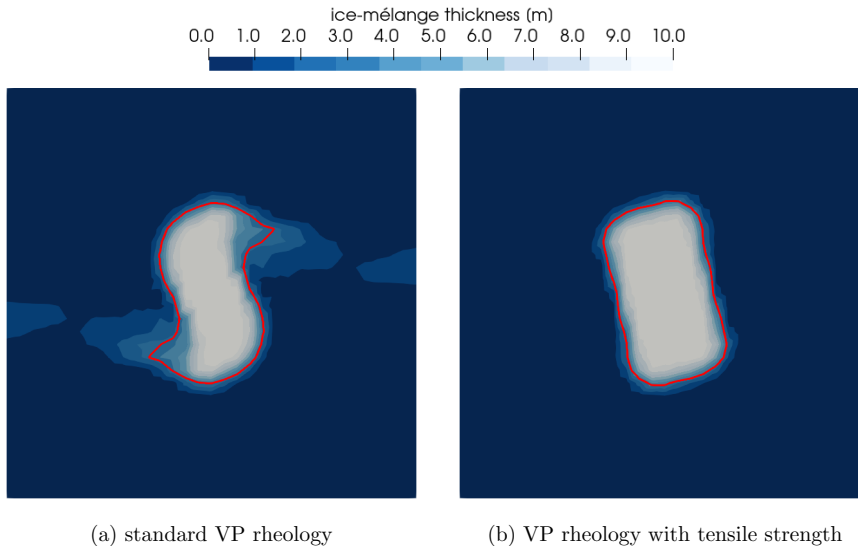
Figure 4. The iceberg is placed under a shearing wind field ($v_{\mathrm{atm}} = \pm\,15\ \mathrm{ms}^{-1}$). Figure 4(a) visualizes the result for the standard viscous-plastic rheology and Figure 4(b) for the viscous-plastic rheology with tensile strength. Both snapshots show the ice-mélange thickness after 3 h. The thick red line shows the iceberg contour.

4.1.3 Iceberg under shear

In the third test case, the same initial setup as in Section 4.1.2 is used. But instead of using a divergent wind field we apply a shearing wind field:

$$v_{\mathrm{atm}} = \begin{cases} 15\ \mathrm{ms}^{-1} & y > 2.5\ \mathrm{km}, \\ -15\ \mathrm{ms}^{-1} & y < 2.5\ \mathrm{km}. \end{cases} \tag{36}$$

The domain of size $5\ \mathrm{km} \times 5\ \mathrm{km}$ is filled with $0.1\ \mathrm{m}$ thick sea ice with a concentration of 0.1. In both cases the iceberg rotates clockwise (see Figure 4) as expected. Using the standard viscous-plastic rheology the iceberg deforms. Figure 4(a) shows that the iceberg contour is slightly s-shaped and parts from the iceberg already detach. This is in contrast to the behaviour of the iceberg using the additional tensile strength (see Figure 4(b)). Here, the iceberg contour stays rectangular and the iceberg rotates as one sea-ice block.

4.2 Particle coupling

The advantage of using a particle method on the joint continuum of sea ice and icebergs is given by the fact that the icebergs and their interactions can be modelled on a subgrid-scale. We consider a domain of size $512\ \mathrm{km} \times 512\ \mathrm{km}$ covered with a quadrilateral mesh of size $16\ \mathrm{km}$. In this setup icebergs are represented by particles with a radius of $125\ \mathrm{m}$. Using this
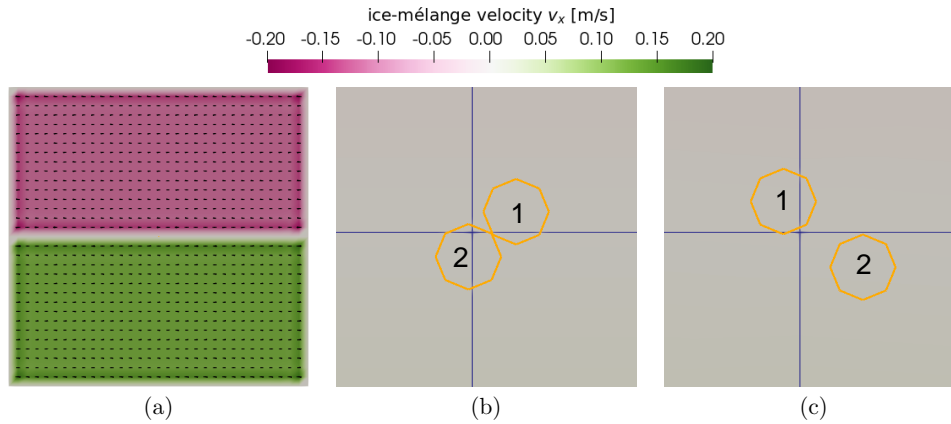
Figure 5. Visualization of the first component of the ice-mélange velocity v for a test case in which two icebergs are transported towards each other by a constant wind ($v_{\text{atm}} = \pm 10 \text{ ms}^{-1}$). Figure (a) shows the whole domain with the initial velocity field. The last two panels show a closeup of the iceberg interaction after (b) 100 time steps and after (c) 200 time steps with a time step of 2000 s.

configuration, we study an iceberg-iceberg interaction under convergent forcing (Section 4.2.1) and analyze the formation of a polynya due to subgrid iceberg grounding (Section 4.2.2). Both test cases use a time step size of 2000 s.

4.2.1 Iceberg-iceberg interaction

An explicit iceberg-iceberg collision is forced in order to test the behaviour of icebergs under contact. Two icebergs with a height of 15 m are placed into a 1 m thick sea-ice field with a concentration of 0.7. The icebergs approach each other due to the following wind field:

$$
v_{\text{atm}} = \begin{cases} 10 \text{ ms}^{-1} & y < 250 \text{ km}, \\ -10 \text{ ms}^{-1} & y > 250 \text{ km}. \end{cases} \tag{37}
$$

The velocity field of the ice mélange after the first time step is shown in Figure 5 (a). At first, the icebergs approach each other until they collide (Figure 5 (b)). Due to collision iceberg 1 moves further up and iceberg 2 further down. After the collision event both icebergs drift past each other and separate again, see Figure 5 (c).

4.2.2 Iceberg grounding

Icebergs can impact sea ice in different ways. For example, mechanically by colliding and breaking up the sea-ice cover, by creating openings and by altering the structure of the sea-ice cover. To simulate such interaction, in the final test case we simulate iceberg grounding. Those grounding events occur in shallow waters and have profound implications for sea-ice dynamics. As icebergs come into contact with the seafloor, they become immobilized, transforming into obstacles that influence

ice mélange concentration

(a) initial setup (b) closeup
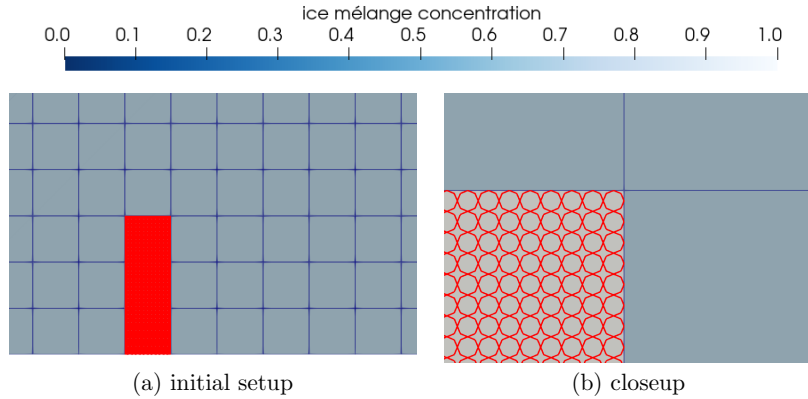
Figure 6. Figure (a) shows the initial ice-mélange concentration of the grounded iceberg setup (lower 2 grid cells). Figure (b) presents a closeup of the upper grid cell so that individual iceberg-particles are visible.

ice-mélange velocity v_x [m/s]

(a) standard VP rheology (b) VP rheology with tensile strength
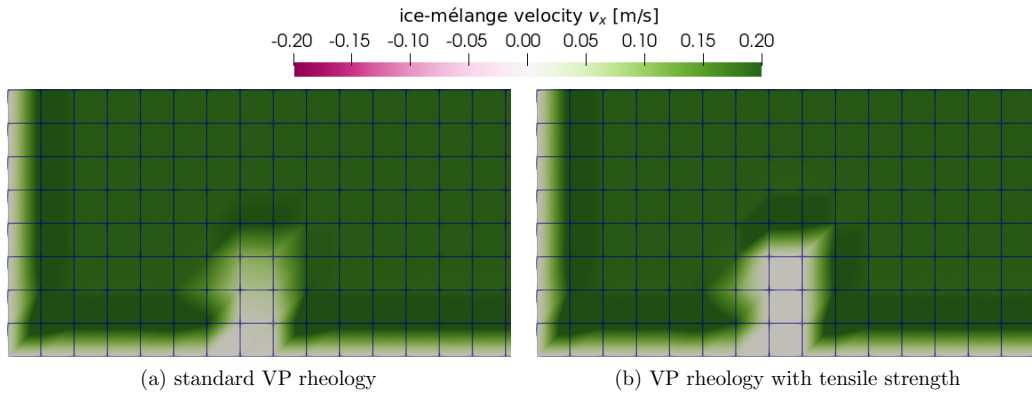
Figure 7. Closeup of the ice-mélange velocity after 5 time steps of the grounded iceberg setup. The area of low velocity in the center of the domain indicates the presence of the icebergs. The ice-mélange is forced by a constant ocean current ($v_{\text{ocean}} = 2\,\text{ms}^{-1}$).

260   the surrounding sea ice. This affects the natural flow and movement of sea ice, and thereby the local circulation patterns and the distribution of sea ice.

In this test case we simulate iceberg grounding and analyze the resulting dynamic of the ice mélange with respect to the formation of a polynya. The domain consists of a 2 m thick sea-ice layer with a concentration of 0.7. Three grid cells, each of the size of 16 km×16 km, are filled with 4096 icebergs per cell (see Figure 6). Each iceberg has a radius of 125 m and is 20 m

265   high. We used such a large number of icebergs to show that we can work with many icebergs per cell that are much smaller than the cell size. These icebergs represent the effects of multiple grounded icebergs in the area with different sizes.

The icebergs in the two lower grid cells closer to the boundary are marked as grounded ($v_{\text{iceberg}} = 0\,\text{ms}^{-1}$). As a forcing we use an ocean current of $v_{\text{ocean}} = 2\,\text{ms}^{-1}$ and neglect any atmospheric forcing ($v_{\text{atm}} = 0\,\text{ms}^{-1}$). Figure 8 (a) shows the grounding event using the standard viscous-plastic rheology. The not grounded icebergs in the upper third cell are transported

(a) standard VP rheology   (b) VP rheology with tensile strength
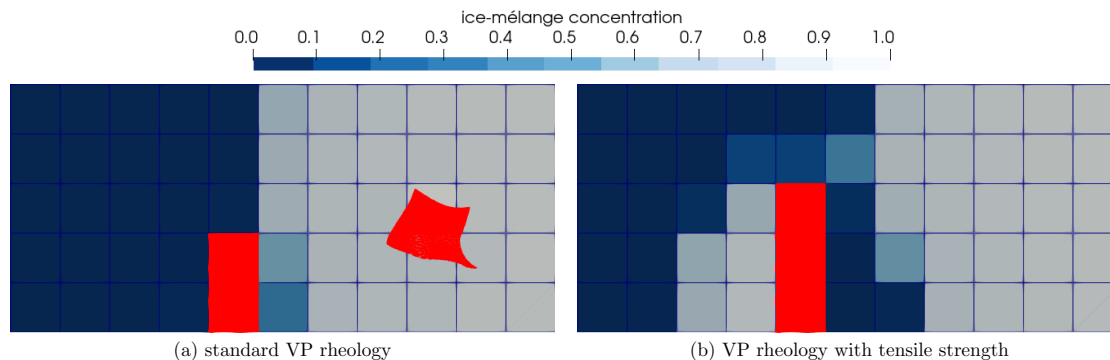
Figure 8. Three grid cells are each filled with 4096 icebergs. The lower two grid cells consists only of grounded icebergs. The snapshots show the ice-mélange concentration after 600 time steps with an ocean forcing of $v_{\text{ocean}} = 2 \text{ ms}^{-1}$.

270   as one block of icebergs towards the right boundary. The square shape is slightly deformed and rotated. The surrounding sea ice accumulated in the domain's right half and builds a straight ice edge. This is a nonphysical behaviour as grounded icebergs should cause a pile-up of sea ice in front of the icebergs. Due to the missing tensile strength in this configuration the ice-mélange velocity is not zero in the dense iceberg field, see Figure 7 (a). Thus, the sea ice flows through the icebergs.

This is in contrast to the results conducted with the modified rheology (see Figure 8 (b)). Here, the additional tensile strength
275   leads to nearly zero velocity in the dense iceberg field (Figure 7 (b)) and prevents the sea ice from passing through the icebergs. Therefore, sea ice accumulates in front of the icebergs. Compared to the setup with the standard viscous-plastic rheology the icebergs do not detach in the configuration with the modified tensile strength. This is due to the fact that the tensile strength for icebergs is present in the upper third grid cell.

5   Discussion

280   In line with prior findings, the results from Section 4 show that a modification of the original sea-ice rheology is crucial to represent icebergs in the viscous-plastic model. In areas with high iceberg coverage, the ice mélange behaves almost like a rigid body due to the modification of the strength parameter.

In order to ensure numerical efficiency, we have represented icebergs on the particle level as round disks. This simplification of the icebergs' geometry obviously effects the simulated iceberg interactions. In addition, the representation via disks requires
285   a uniform iceberg thickness, which may lead to a coarse approximation of the forces in the ice mélange. Since we model the iceberg interaction on a subgrid-scale and integrate the icebergs into the large scale sea-ice model, the impact of these simplifications is of second order.

Concerning the response of the ice mélange due to subgrid iceberg grounding, we note that polynyas, which can be simulated in the ice mélange, cannot be smaller than the size of a grid cell, as in any standard sea-ice model. Furthermore, the presence
290   of tensile strength in a grid cell depends on a certain coverage of a grid cell with icebergs. The used threshold $A_{\text{icebergs}} <$

$\pi \frac{(0.5\sqrt{|K|})^2}{|K|}$ is motivated by the grounded iceberg test case and should be evaluated and further adjusted in more realistic setups.

Another assumption that could be relaxed in our ice-mélange model is the usage of uniform drag coefficients for ocean and air. Instead, different values for sea ice and icebergs could be applied. So far, the applied particle realization also does not represent mechanical break off of an iceberg or mechanical bonding of two icebergs. Implementing these processes is subject to future work.

6 Conclusions

We present a prototype of a dynamic hybrid ice-mélange model, which can be straight forwardly coupled to existing sea-ice components in climate models. The ice mélange is described as a joint continuum of sea ice and icebergs. While sea ice is represented as a continuum, the icebergs are modelled by particles. In order to derive a joint continuum for the ice-mélange's thickness and concentration, we integrate the particles into the sea-ice thickness and sea-ice concentration. By doing so, icebergs in the ice mélange are considered as thick and compact pieces of sea ice.

Due to the use of particles in the joint continuum, we do not need to use meshes that resolve icebergs (< 300 m) in the ice mélange. Instead, the ice-mélange model can be simulated on the mesh resolution used for sea-ice components in climate models. This is an appealing feature with respect to the numerical efficiency.

In the context of the hybrid ice-mélange model, sea ice is modelled based on a modification of the continuum viscous-plastic sea-ice rheology, which is currently the most used material law for sea ice in climate models. Icebergs are introduced into the viscous-plastic rheology by a strength parameterization, which is used in order to prevent icebergs from diffusing. The hybrid model is validated through a series of idealized setups that represent situations observed in nature. The setups demonstrate that the integrated icebergs, represented as thick and compact pieces of sea ice, maintain their shape under high pressure or difficult wind conditions due to the strength modification. Furthermore, we show that the hybrid ice-mélange model is capable of simulating a polynya due to subgrid iceberg grounding. These examples highlight situations where this modelling framework is beneficial. These are setups where the sea-ice cover is dense and the geometry of the fjord is complex such that sea-ice-iceberg interactions are important.

In conclusion, the use of particles and the simple extension of the viscous-plastic sea-ice material law makes the hybrid model a promising approach to efficiently integrate ice-mélange into climate models.

Code and data availability. The model code used for the numerical examples are freely available from https://doi.org/10.5281/zenodo.7767470. The source code of Gascoigne is available to individuals (https://gascoigne.math.uni-magdeburg.de/index.php?show=downloadinstallation).

Author contributions. SK worked on the implementation. SK and CM worked on the model development and analysis of the model. All the authors contributed to writing.

Competing interests. The authors declare that they have no conflict of interest.

Acknowledgements. CM acknoweledges funding by the Deutsche Forschungsgemeinschaft (DFG, German Research Foundation) - Project number 463061012. DN acknowledges funding by the DFG under Germany's Excellence Strategy - EXC 2037 'CLICCS - Climate, Climatic Change, and Society' - Project Number: 390683824.

320

References

Amundson, J. M. and Burton, J. C.: Quasi-static granular flow of ice mélange, J. Geo. Res., 123, 2243–2267, https://doi.org/10.1029/2018JF004685, 2018.

Amundson, J. M., Fahnestock, M., Truffer, M., Brown, J., Lüthi, M. P., and Motyka, R. J.: Ice mélange dynamics and implications for terminus stability, Jakobshavn Isbræ, Greenland, J. Geophys. Res., 115, F01 005, https://doi.org/10.1029/2009JF001405, 2010.

Amundson, J. M., Robel, A. A., Burton, J. C., and Nissanka, K.: A quasi-one-dimensional ice mélange flow model based on continuum descriptions of granular materials, EGUsphere, 2024, 1–26, https://doi.org/10.5194/egusphere-2024-297, 2024.

Bassis, J., Berg, B., Crawford, A., and Benn, D.: Transition to marine ice cliff instability controlled by ice thickness gradients and velocity, Science, 372, 1342–1344, https://doi.org/0.1126/science.abf6271, 2015.

Bevan, S. L., Luckman, A. J., Benn, D. I., Cowton, T., and Todd, J.: Impact of warming shelf waters on ice mélange and terminus retreat at a large SE Greenland glacier, The Cryosphere, 13, 2303–2315, https://doi.org/10.5194/tc-13-2303-2019, 2019.

Braack, M., Becker, R., Meidner, D., Richter, T., and Vexler, B.: The Finite Element Toolkit Gascoigne, https://doi.org/10.5281/ZENODO.5574969, www.gascoigne.de, 2021.

Burton, J. C., Amundson, J. M., Cassottoc, R., Kuod, C.-C., and Dennin, M.: Quantifying flow and stress in ice mélange, the world's largest granular material, P. Natl. A. Sci., 115, 5105–5110, https://doi.org/10.1073/pnas.1715136115, 2018.

Cassotto, R., Fahnestock, M., Amundson, J. M., Truffer, M., and Joughin, I.: Seasonal and interannual variations in ice melange and its impact on terminus stability, Jakobshavn Isbræ, Greenland, J. Glaciol., 61, 76–88, https://doi.org/10.3189/2015JoG13J235, 2015.

Coon, M. D.: A review of AIDJEX modeling. In Sea Ice Processes and Models: Symposium Proceedings, University of Washington Press, Seattle, 1980.

Davison, B., Cowton, T.R.and Cottier, F., and Sole, J.: Iceberg melting substantially modifies oceanic heat flux towards a major Greenlandic tidewater glacier, Nat. Commun., 11, https://doi.org/10.1038/s41467-020-19805-7, 2020.

Dowdeswell, J. A., Whittington, R. J., and Hodgkins, R.: The Sizes, Frequencies, and Freeboards of East Greenland Icebergs Observed Using Ship Radar and Sextant, J Geophys. Res., 97, 3515–3528, https://doi.org/10.1029/91JC02821, 1992.

Enderlin, E. M., Carrigan, C. J., Kochtitzky, W. H., Cuadros, A., Moon, T., and Hamilton, G. S.: Greenland iceberg melt variability from high-resolution satellite observations, The Cryosphere, 12, 565–575, https://doi.org/10.5194/tc-12-565-2018, 2018.

Flato, G. M. and Hibler, W. D.: Modelling Pack Ice as a Cavitating Fluid, J. Phys. Oceanogr., https://doi.org/0.1175/1520-0485(1992)022<0626:MPIAAC>2.0.CO;2, 1992.

Herman, A.: Molecular-dynamics simulation of clustering processes in sea-ice floes, Physical Review E, 84, 2011.

Hibler, W. D.: A Dynamic Thermodynamic Sea Ice Model, J. Phys. Oceanogr., 9, 815–846, https://doi.org/10.1175/1520-0485(1979)009<0815:ADTSIM>2.0.CO;2, 1979.

Hirt, C. W. and Nichols, B. D.: Volume of Fluid (VOF) Method for the Dynamics of Free Boundaries, Journals of Computational Physics, 39, 201–225, https://doi.org/10.1016/0021-9991(81)90145-5, 1982.

Hunke, E.: Viscous-Plastic Sea Ice Dynamics with the EVP Model: Linearization Issues, Journal of Computational Physics, 170, 18–38, https://doi.org/10.1006/jcph.2001.6710, 2001.

Ip, C. F., Hibler, W. D., and Flato, G. M.: On the effect of rheology on seasonal sea-ice simulations, Ann. Glaciol., 15, 17–25, https://doi.org/10.3189/1991AoG15-1-17-25, 1991.

Koldunov, N., S.Danilov, Sidorenko, D., Hutter, N., Losch, M., Goessling, H., Rakowsky, N., Scholz, P., Sein, D., Wang, Q., and Jung, T.: Fast EVP Solutions in a High-Resolution Sea Ice Model, Journal of Advances in Modeling Earth Systems, 11, 1269–1284, https://doi.org/https://doi.org/10.1029/2018MS001485, 2019.

Kreyscher, M., Harder, M., Lemke, P., and Flato, G. M.: Results of the Sea Ice Model Intercomparison Project: Evaluation of sea ice rheology schemes for use in climate simulations, J Geophys. Res.-Oceans, 105, 11 299–11 320, https://doi.org/10.1029/1999JC000016, 2000.

Krug, J., Durand, G., Gagliardini, O., and Weiss, J.: Modelling the impact of submarine frontal melting and ice melange on glacier dynamics, Cryosphere, 9, 989–1003, 2015.

König, B. C. and Holland, D. M.: Modeling landfast sea ice by adding tensile strength, J. Phys. Oceanogr., 40, 185–198, https://doi.org/10.1175/2009JPO4105.1, 2010.

Leppäranta, M.: The drift of Sea Ice, Springer-Verlag Berlin Heidelberg, 2011.

Mehlmann, C. and Richter, T.: A finite element multigrid-framework to solve the sea ice momentum equation, Journal of Computational Physics, 384, 847–861, 2017a.

Mehlmann, C. and Richter, T.: A modified global Newton solver for viscous-plastic sea ice models, Ocean Model., 116, 96–107, https://doi.org/10.1016/j.ocemod.2017.06.001, 2017b.

Moon, T., Sutherland, D., Carroll, D., Felikson, D., Kehrl, L., and Straneo, F.: Subsurface iceberg melt key to Greenland fjord freshwater budget, Nature Geosci., 11, 49–45, https://doi.org/10.1038/s41561-017-0018-z, 2018.

Mortensen, J., Rysgaard, S., Bendtsen, J., Lennert, K., Kanzow, T., Lund, H., and Meire, L.: Subglacial Discharge and Its Down-Fjord Transformation in West Greenland Fjords With an Ice Mélange, Journal of Geophysical Research: Oceans, 125, e2020JC016 301, https://doi.org/https://doi.org/10.1029/2020JC016301, 2020.

Pollard, D., DeConto, R. M., and Alley, R. B.: A continuum model (PSUMEL1) of ice mélange and its role during retreat of the Antarctic Ice Sheet, Geosci. Model Dev., 11, 5149–5172, https://doi.org/10.5194/gmd-11-5149-2018, 2018.

Robel, A.: Thinning sea ice weakens buttressing force of iceberg mélange and promotes calving, Nat. Commun., p. 7, https://doi.org/10.1038/ncomms14596, 2017.

Schlemm, T. and Levermann, A.: A simple parametrization of mélange buttressing for calving glaciers, The Cryosphere, 15, 531–545, https://doi.org/10.5194/tc-15-531-2021, 2021.

Shen, H., Hibler, W., and Leppäranta, M.: The role of floe collisions in sea ice rheology, J. Geophys. Res.: Oceans, 92, 7085–7096, 1987.

Stroeve, J., Barrett, A., Serreze, M., and Schweiger, A.: Using records from submarine, aircraft and satellites to evaluate climate model simulations of Arctic sea ice thickness, The Cryosphere, 8, 1839–1854, https://doi.org/10.5194/tc-8-1839-2014, 2014.

Sulak, D., Sutherland, D., Enderlin, E., Stearns, L., and Hamilton, G.: Iceberg properties and distributions in three Greenlandic fjords using satellite imagery, Ann. Glaciol., 58, 92–106, https://doi.org/10.1017/aog.2017.5, 2017.

Vaňková, I. and Holland, D.: A Model of Icebergs and Sea Ice in a Joint Continuum Framework, J Geophys. Res.-Oceans, 122, 9110–9125, https://doi.org/10.1002/2017JC013012, 2017.

Xie, S., Dixon, T., Holland, D., Voytenko, D., and Vaňková, I.: Rapid iceberg calving following removal of tightly packed pro-glacial mélange, Nat Commun 10, https://doi.org/10.1038/s41467-019-10908-4, 2019.